

Lawrence Berkeley National Laboratory

Recent Work

Title

Highly Permeable Perfluorinated Sulfonic Acid Ionomers for Improved Electrochemical Devices: Insights into Structure-Property Relationships.

Permalink

<https://escholarship.org/uc/item/0rh082p6>

Journal

Journal of the American Chemical Society, 142(8)

ISSN

0002-7863

Authors

Katzenberg, Adlai
Chowdhury, Anamika
Fang, Minfeng
et al.

Publication Date

2020-02-01

DOI

10.1021/jacs.9b09170

Peer reviewed

Highly Permeable Perfluorinated Sulfonic Acid Ionomers for Improved Electrochemical Devices: Insights into Structure - Property Relationships

Adlai Katzenberg^{1,2}, Anamika Chowdhury², Minfeng Fang¹, Adam Z. Weber²,

Yoshiyuki Okamoto¹, Ahmet Kusoglu², and Miguel A. Modestino¹

¹Tandon School of Engineering, New York University, Brooklyn, 11201, NY

²Lawrence Berkeley National Laboratory, Berkeley, 94720, CA

Abstract

Rapid improvements in polymer-electrolyte fuel-cell (PEFC) performance have been driven by the development of commercially available ion-conducting polymers (ionomers) that are employed as membranes and catalyst binders in membrane-electrode assemblies. Commercially available ionomers are based on a perfluorinated chemistry comprised of a polytetrafluoroethylene (PTFE) matrix that imparts low gas permeability and high mechanical strength but introduces significant mass-transport losses in the electrodes. These transport losses currently limit PEFC performance, especially for low Pt loadings. In this study, we present a novel ionomer incorporating a glassy amorphous matrix based on a perfluoro(2-methylene-4-methyl-1,3-dioxolane) (PFMMD) backbone. The novel backbone chemistry induces structural changes in the ionomer, restricting ionomer domain swelling under hydration while disrupting matrix crystallinity. These structural

changes slightly reduce proton conductivity while significantly improving gas permeability. The performance implications of this tradeoff are assessed, which reveal the potential for substantial performance improvement by incorporation of highly permeable ionomers as the functional catalyst binder. These results underscore the significance of tailoring material chemistry to specific device requirements, where ionomer chemistry should be rationally designed to match the local transport requirements of the device architecture.

Introduction

The thrust to develop efficient solutions for energy conversion has produced substantial improvements in polymer-electrolyte fuel-cell (PEFC) performance in the past decades¹. These improvements have largely been driven by the remarkable transport properties of a class of perfluorinated ion-conducting polymers, or ionomers^{2,3}. A range of perfluorinated sulfonic-acid (PFSA) ionomers are commercially available and share two key chemical components: a PTFE backbone and a sulfonic-acid pendant side chain^{4,5}. The PTFE backbone microphase separates from the sulfonic-acid side chains, leading to a network of interconnected hydrophilic ion-conducting domains in a hydrophobic semicrystalline matrix⁶⁻¹⁰. Crystallites in the PTFE matrix reduce fractional free volume (FFV), add tortuosity, and ultimately limit gas diffusion through the matrix^{5,11-17}. These structural properties give traditional PFSAs the remarkable ionic conductivity and low gas permeability that make them ideal PEFC membranes. The same ionomers are often employed as the catalyst binder in the electrodes, despite the different transport requirements. While membranes require low permeability to limit crossover of fuel (oxygen and hydrogen gas), the catalyst binder requires high gas permeability to maximize the flux of these gaseous species to active catalyst sites. It is widely

believed that PEFC power density is limited by oxygen mass transport to the local reaction site in the cathode^{2,18,19}, due to the low permeability of the ionomer catalyst binder¹⁵⁻¹⁷. These limitations are exacerbated by changes in transport properties and structure of the ionomer confined to nanometer thicknesses in the catalyst layers²⁰.

A promising strategy to lower the gas-transport resistance in catalyst layers is the development of ionomer binders with enhanced gas permeability. Such materials design strategies include substituting the linear PTFE backbone of state-of-the-art PFSA ionomers with different substituents²¹ or side-chains²² that disrupt the crystallinity of the matrix and increase its FFV. Previous work on perfluorinated membranes demonstrated that asymmetric dioxolane homopolymers, poly[perfluoro(2-methylene-4-methyl-1,3-dioxolane)] or poly(PFMMD), exhibit an amorphous internal morphology with high FFV (*i.e.* 0.23)²³, which results in gas permeabilities (*i.e.* ~240 barrer for hydrogen) that are an order of magnitude higher than PTFE homopolymers^{24,25}. Work on dioxolane-derived polymers derived from copolymerization of PFMMD with other perfluorinated vinyl monomers^{26,27} inspired our current study where we explore a new family of perfluorinated ionomers composed of PFMMD-co-PFSA copolymers, where the PFMMD matrix is designed to provide an amorphous domain for fast gas permeation while the PFSA ionomer domains provide pathways for proton conduction (Figure 1). This strategy aims to deconvolute the transport pathways for proton- and gas-transport by rational molecular design.

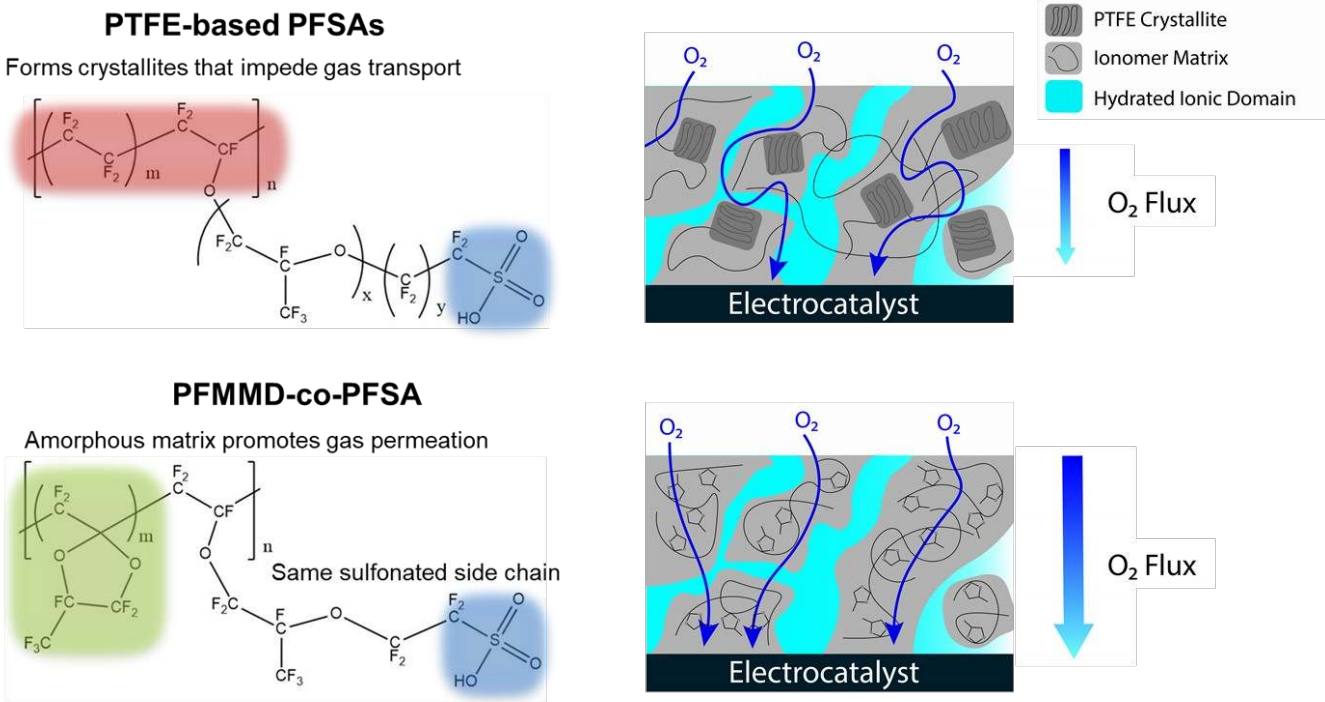
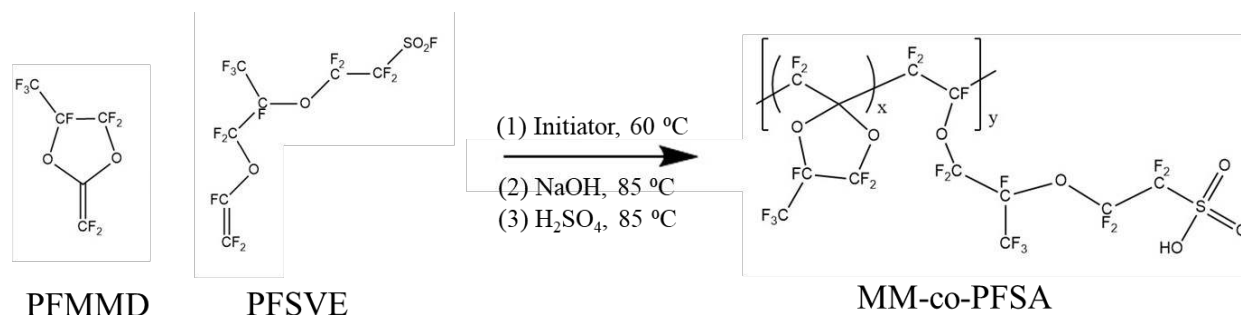


Figure 1: Traditional PFSA[®] such as Nafion[®] (top) consist of a semicrystalline PTFE matrix and a sulfonated pendant side chain. Crystallinity in the matrix results in low gas permeability, which induces substantial mass-transport limitations in fuel cells. PFMMD-co-PFSA (bottom), a novel ionomer developed at New York University, incorporates an amorphous dioxolane group in the matrix to disrupt crystallinity and improve gas permeability. The ionomer contains the same characteristic sulfonated side chain to preserve the mechanism for ion conduction in traditional PFSA[®]s.

The synthesis of PFMMD-co-PFSA proceeds via a facile liquid-phase free radical polymerization of PFMMD and perfluoro(4-methyl-3,6-dioxaoct-7-ene) sulfonyl fluoride (PFSVE) under mild conditions, followed by the hydrolysis of the resulting sulfonyl fluoride (Scheme 1). This facile two-step synthesis route provides us unprecedented control over the ionomer composition and enables a systematic study of the relationship between molecular design, nanostructure, and transport properties. By exploring the impact of matrix chemistry and sulfonic-acid concentration on key transport properties (ionic conductivity and gas permeability) we offer insights into the role of the molecular design in ionomer performance and demonstrate the potential for rational design of the next generation of functional catalyst binders.



Scheme 1: PFMMD-co-PFSA is prepared by free radical polymerization of PFMMD and PFSVE in a sealed reaction ampoule with a fluorinated initiator. The polymer composition can be tuned by the ratio of PFMMD and PFSVE in the reaction feed stock. After free-radical polymerization, the sulfonated side-chain is converted from the sulfonyl fluoride ($-\text{SO}_2\text{F}$) to sulfonic acid ($-\text{SO}_3\text{H}$) form by base hydrolysis followed by protonation.

Results and Discussion

Synthesis of PFMMD-co-PFSA Ionomers

In the binary copolymerization of PFMMD and PFSVE, the ionomer composition is determined by the mole fractions of each monomer in the reaction solution. This composition varies with conversion and reactivity ratios, which describe the relative rate constants for the incorporation of each monomer (Figure 2). The reactivity ratios, r_{PFMMD} and r_{PFSVE} , are system-dependent constants that must be determined to predict and control ionomer composition. Reactivity ratios were determined by performing a series of polymerization with varying feedstock compositions and measuring the resulting incorporation of the monomers into the polymer by elemental analysis (Figure 2). Reactivity ratios were extracted from Equation 2.

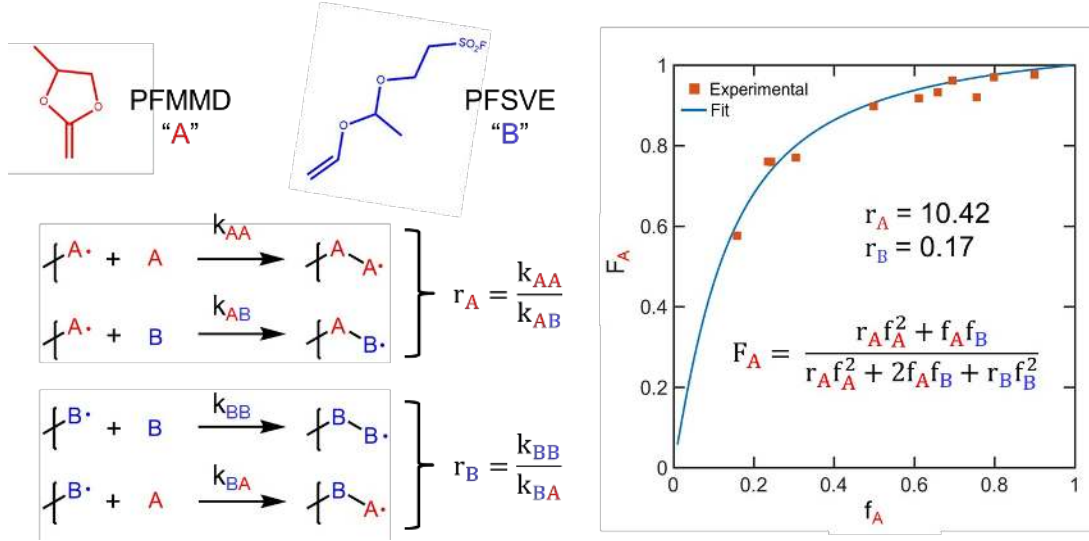


Figure 2: Four reactions occur simultaneously during chain propagation in binary free-radical copolymerization (left). Each of these reactions has a characteristic rate constant, k_{ij} . The ratios of these constants, r_{ij} , describe the probability of each monomer incorporating into growing chains. For copolymerization of PFMMD (represented as "A") and PFSVE (represented as "B"), $r_A > 1 > r_B$. This disparity in reactivity ratios induces compositional drift as the feedstock changes throughout the course of the reaction.

The consumption of each monomer i or j is given by:

$$\frac{-d[M_i]}{dt} = k_{ii}[M_i][M_i^\bullet] + k_{ji}[M_i][M_j^\bullet] + k_{xi}[M_i][X] \quad \text{(Equation 1)}$$

where $i \neq j$, $[M_i]$ is the concentration of monomer i , k_{ii} is the respective rate constant, $[M_i^\bullet]$ is the concentration of active centers, and $[X]$ is the initiator concentration. By assuming that the concentration of radical intermediates is at steady state ($d[M_1^\bullet]/dt = d[M_2^\bullet]/dt = 0$), the copolymer composition equation becomes^{28,29}:

$$F_i = \frac{d[M_i]}{d[M_i] + d[M_j]} = \frac{r_i f_i^2 + f_i f_j}{r_i f_i^2 + 2 f_i f_j + r_j f_j^2} \quad \text{(Equation 2)}$$

where $r_i = k_{ii}/k_{ij}$, f_i is the mole fraction of monomer i in the feed, and F_i is the mole fraction of monomer i in the polymer. For the case of PFMMD-co-PFSVE, it was found that $r_{\text{PFMMD}} > 1 > r_{\text{PFSVE}}$. This indicates a much higher probability of growing chains to incorporate PFMMD over PFSVE. As a result, the relative concentration of PFMMD in the reaction solution will decrease over the course of the polymerization with

respect to PFSVE, leading to compositional drift in the polymer chains. This implies that chains which grow early in the reaction will encounter higher f_{PFMMD} than chains which grow at a later stage. The resulting polymer is a blend of chains with different compositions reflecting the changing feedstock. As proton transport in ionomers arises from their complex phase-separated nanostructure, which, in turn, is dictated by the overall polymer composition and the distribution of monomers in the chains, it was important to develop a polymerization model to guide the synthesis and achieve control over the degree of compositional drift. While equation 2 provides a description of the instantaneous polymer composition, the control of the synthesis over time required an integral polymerization model capable of predicting the monomer incorporation as a function of conversion. In terms of conversion, the polymer composition is given by

$$F_i = \frac{1}{[M]_0} \frac{d[M_i]}{dX} \quad \text{(Equation 3)}$$

where $[M]_0$ is the initial total monomer concentration. Given that the differential conversion dX can be expressed in terms of the monomer concentration change

$$dX = \frac{d[M_i] + d[M_j]}{[M]_0} \quad \text{(Equation 4)}$$

and following the analysis by Skeist³⁰ and Meyer and Lowry³¹, we can derive that the differential copolymer composition is given by

$$\frac{dX}{df_i} = (X-1) \left(\frac{\alpha}{f_i} - \frac{\beta}{1-f_i} - \frac{\gamma}{f_i - \delta} \right) \quad \text{(Equation 5)}$$

where

$$\alpha = \frac{r_j}{1-r_j} \quad \beta = \frac{r_i}{1-r_i} \quad \gamma = \frac{1-r_i r_j}{(1-r_i)(1-r_j)} \quad \delta = \frac{1-r_j}{2-r_i-r_j}$$

Integrating equation (5) allows predicting the feed (f_i) and polymer (F_i) compositions as a function of conversion. The integration results, shown in Figure 3(a), demonstrate that the composition changes drastically throughout the course of a reaction. For feed stocks containing greater than 20 mol% PFMMMD, the polymer initially incorporates at least 80 mol% PFMMMD, but this incorporation rapidly drops to ~ 0 mol% as PFMMMD becomes depleted. To visualize the impact of the dynamic change in monomer incorporation better, the simulated compositional drift is shown in Figure 3(b), described as the deviation of the polymer composition (in mole fraction) from its initial value at $X = 0$. This figure can be interpreted as a synthesis phase diagram with three distinct regions; the low-drift (blue) region, where monomers are statistically distributed across propagating chains; the drift-onset region, where the matrix monomer becomes depleted and compositional drift becomes significant; and the severe-drift (red) region where the matrix monomer is fully depleted and only PFSVE is available for reaction.

A key observation from the compositional drift model is that the drift onset occurs at very low conversions for low f_{PFMMD} , or high fractions of the sulfonated monomer in the feed. Given the low reactivity of PFSVE, high feed fractions are required to achieve sufficient incorporation of sulfonic acid in the final product. To access the high PFSVE regions while ensuring statistical distribution of monomers, all syntheses (shown as white triangles in Figure 3(b)) were terminated prior to reaching the drift-onset region.

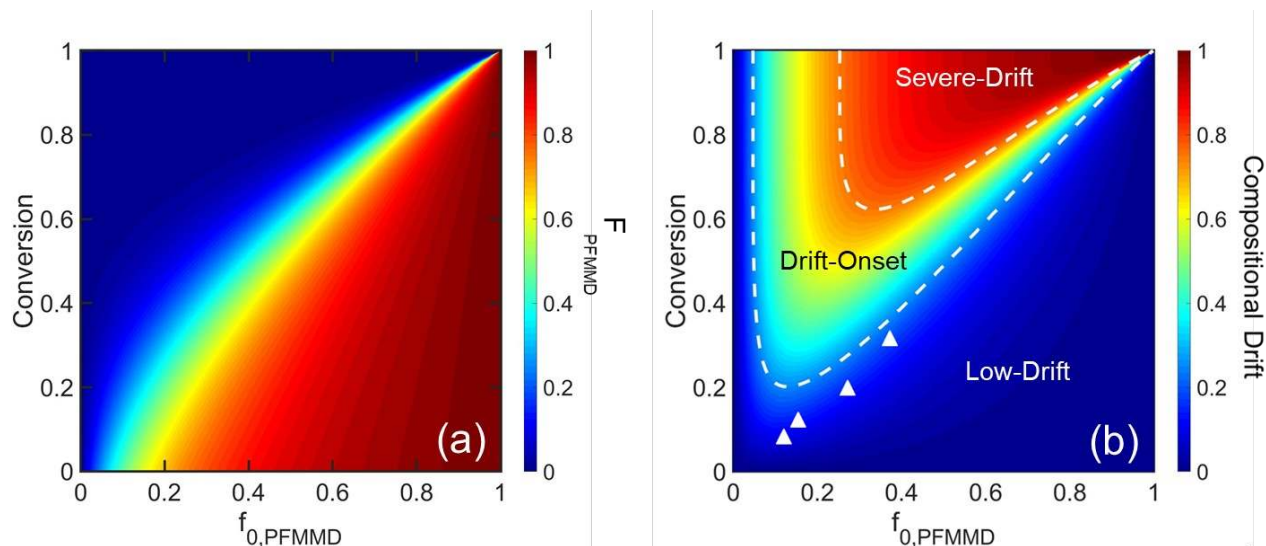


Figure 3: Numerical simulation of compositional drift in the copolymerization of PFMMMD and PFSVE. (a) Polymer composition, F_{PFMMD} , for a given feed composition, f_{PFMMD} , changes with conversion. (b) This can be expressed as the magnitude of compositional drift, or the change in F_{PFMMD} from its initial value. Compositional drift becomes especially severe for low f_{PFMMD} , which introduces challenges in reaching high PFSVE fractions in the copolymer while maintaining statistical distribution of monomers. White triangles indicate the synthesis batches used to generate a range of statistical ionomer compositions.

Nanostructure and Ionic Conductivity

Using a series of PFMMMD-co-PFSA copolymers with controlled composition allows for development of the relationships between chemical design, structure, and transport properties. It should be noted that the water sorption and proton conductivity measurements presented here are of thin-films supported on planar substrates. It is well known that these and other properties of PFSA ionomers (e.g. Nafion) may change when the polymer is confined from bulk to nanometer thicknesses. To avoid convoluting confinement with chemical-composition effects, the thicknesses used in this study were chosen well above the typical benchmark thickness for confinement in ionomers (*i.e.*, >50 nm)⁵. Further detail on the measurement techniques and confinement considerations can be found in the supporting information.

First, we characterized the ionic conductivity of PFMMD-co-PFSA ionomers through electrochemical impedance spectroscopy (EIS) on a set of polymers with PFSA mass fractions ranging from 0.26 to 0.57 at relative humidity values of 23%, 43%, 75%, and 97% (Figure 5a). As with state-of-the-art PFSA ionomers, proton conductivity was highly sensitive to hydration and concentration of ionic groups in the polymer. This is consistent with current understanding of the mechanism of ion conduction of PFSAs, which is governed by the hydration of the ionic domains and their interconnectivity at longer length scales^{5,7,8,32}. As water diffuses into these domains, they swell to form a percolated network of channels that act as pathways for proton transport. The extent of swelling is determined by a chemical/mechanical energy balance where the chemical potential of water in the external reservoir is in equilibrium with the water in the ionic domains of the polymer that considers the change in the free energy induced in the polymer by swelling. Increasing the sulfonic-acid concentration shifts this equilibrium toward higher hydration states by decreasing the chemical potential of water in the ionomer and thus allowing for higher water uptake.

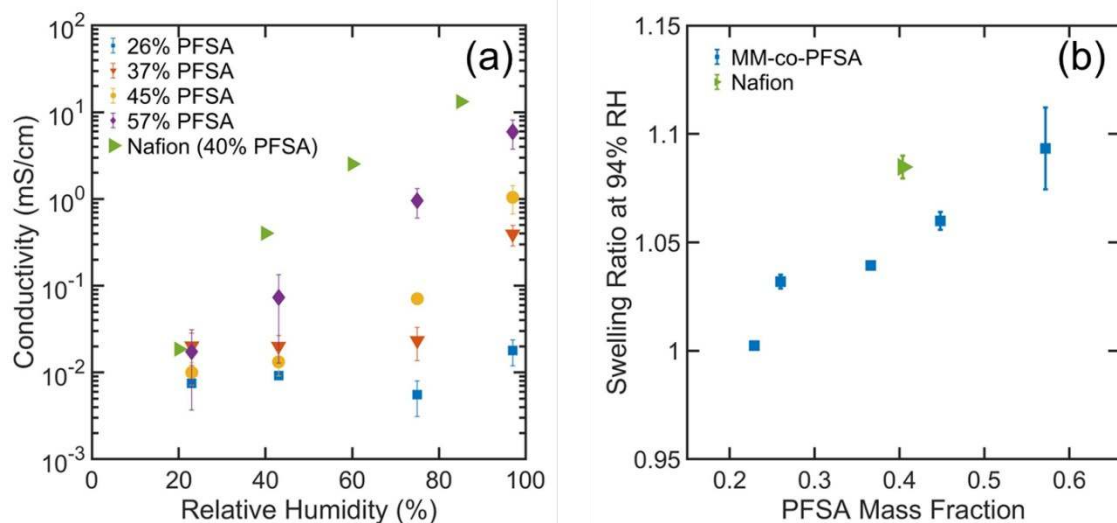


Figure 4: (a) Proton conductivity (measured by EIS) and (b) water sorption (measured by ellipsometry) of PFMMD-co-PFSA thin-films are sensitive to the mass fraction of sulfonic-acid groups. At high PFSA fraction, the ionic conductivity of PFMMD-co-PFSA approaches that of Nafion. However, it remains lower by a factor of 2, even at higher PFSA fractions than Nafion 1100. Nafion data reproduced from reference 33. (b) Water sorption of PFMMD-co-PFSA thin films shows similar dependence on PFSA fraction as the ionic conductivity. PFMMD-co-PFSA swells less at a given PFSA fraction than Nafion.

At high hydration, the highest PFSA fraction (0.57) approached the conductivity of Nafion (0.4 PFSA fraction) but remained lower by a factor of two, despite the higher PFSA fraction. This behavior can be explained by the glassy matrix of PFMMD-co-PFSA copolymers, which imposes a higher resistance to deformation during swelling and is consistent with the swelling measurements presented in Figure 5b. The equilibrium swelling fraction at high humidity was strongly dependent on PFSA fraction, as higher ionic strength in the polymer increases the driving force for water sorption. However, PFMMD-co-PFSA exhibited reduced swelling compared to Nafion at comparable PFSA fraction due to the higher stiffness of the former imparted by its glassy matrix.

Ion conduction and water sorption in PFSA ionomers are strongly connected to the material's nanostructure. To gain further insights into the morphological effects on the macroscopic transport behavior, small-angle X-ray scattering (SAXS)

was used to probe the effect of the incorporation of the PFMMD backbone on the nanostructure of the copolymers. The morphology in hydrated PFSA ionomers and swelling of their ionic domains has been widely studied by SAXS^{8,32,34}. State-of-the-art PFSA ionomers exhibit two characteristic features in their SAXS profiles; an ionomer peak (scattering vector q between 1 and 2.5 nm⁻¹) corresponding to the spatial correlation between ionic domains and a broad matrix peak (0.2 nm⁻¹ to 1 nm⁻¹) corresponding to the inter-crystallite spatial correlation⁵. Higher hydration levels and PFSA fractions results in a shift in the position of the ionomer peak to lower q -values due to the increased hydrophilic domain spacing. Similar to Nafion, SAXS profiles for PFMMD-co-PFSA ionomers equilibrated in water show a single broad peak at q -values close to 2 nm⁻¹. The position of this peak shifts to lower q -values as the PFSA fraction increases, suggesting that it arises from the correlation between ion-conducting domains in the polymers. This shift coincides with decreased peak breadth, which suggests increased domain connectivity and lower tortuosity at higher PFSA fractions. Furthermore, the characteristic spacing of these domains (Figure 6b) were consistently smaller (and slightly broader) than those of Nafion^{5,32}. The smaller and more tortuous nano-domains inferred from SAXS, along with the reduction in macroscopic water uptake, is expected to result in smaller and more tortuous pathways for ion transport, thereby reducing the proton conductivity.

Additionally, SAXS profiles for PFMMD-co-PFSA ionomers do not exhibit the characteristic matrix peak observed in Nafion, suggesting that the incorporation of asymmetric dioxolane groups in the backbone disrupts the crystallinity of the material leading to an amorphous matrix. To confirm the loss in crystallinity, wide-angle X-ray scattering (WAXS) profiles for PFMMD-co-PFSA ionomers are presented

in Figure 6(c) are similar to the PFMMD homopolymer²⁵ and demonstrate the loss of the PTFE crystallite peak, present in Nafion at $q = 8$ to 16 nm^{-1} .

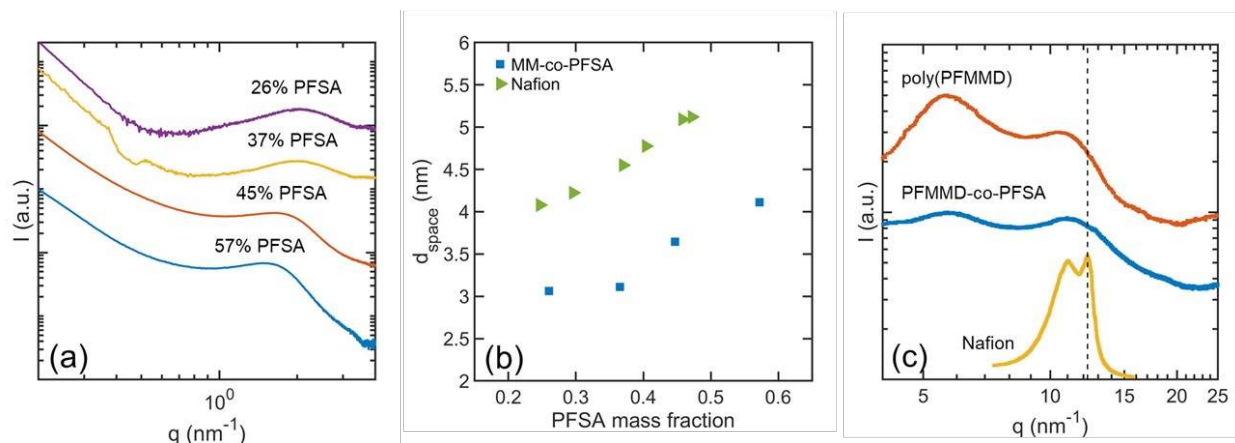


Figure 5: (a) SAXS profiles of hydrated PFMMD-co-PFSA at PFSA mass fractions ranging from 0.26 to 0.57. A scattering peak is present at q values close to 2 nm^{-1} , close to the ionomer peak of hydrated Nafion. As PFSA fraction increases, the intensity of this peak increases as it shifts to lower q values, indicating larger ionomer domains. (b) Ionomer domain spacing is shown for Nafion (green, from reference 5 as reproduced from reference 32) and PFMMD-co-PFSA (blue) for a range of PFSA mass fractions, as calculated from SAXS scattering peaks. The domain spacings of the two ionomers exhibit a similar dependence on PFSA fraction, with PFMMD-co-PFSA displaying domains around 1 nm smaller than Nafion. (c) The WAXS profile of PFMMD-co-PFSA (0.37 PFSA mass fraction) shows similar matrix structure to the poly(PFMMD) homopolymer. Notably, the PTFE crystalline peak (denoted by dashed line) is absent. Nafion WAXS profile reproduced from reference 35, and poly(PFMMD) from reference 25.

Gas-Transport Properties

While the incorporation of a glassy matrix reduced ionic conductivity in PFMMMD-co-PFSA by constricting ionomer domains, its amorphous nature could lead to an increase in gas permeability¹⁴. Two key polymer properties that dictate gas permeability are free volume and chain mobility. While PTFE itself has low mobility as indicated by its high T_g (115°C)³⁶, its thermal-mechanical properties change when incorporated in an ionomer. PFSA ionomers display multiple thermal transitions that arise from different molecular origins: the β -transition, associated with segmental motion of the main-chain, occurs between -40 and 20°C, indicating the matrix is rubbery and has high mobility at room temperature³⁷. In contrast, the T_g of PFMMMD homopolymers is 135°C, indicating lower mobility than PTFE. This value is expected to change when PFMMMD is copolymerized with PFSA, as segmental motion is known to be affected by ionic interactions between sulfonate groups and cations. The role of ionic interactions is complex due to their dependence on hydration state, cation nature, and film thickness³⁸, making it difficult to isolate the contribution of matrix chemistry to transition temperature. To decouple the role of matrix mobility from the ionic interactions present in the ionomers, we explored the materials thermal transitions in the neutral sulfonyl-fluoride (SO₂F) form. Differential-scanning calorimetry (DSC) measurements demonstrated a single thermal transition in PFMMMD-co-PFSF (the SO₂F precursor of PFMMMD-co-PFSA) (Figure 7). The temperature of this transition decreased with increasing PFSF mole fraction, indicating higher mobility of the sulfonated side chain than the dioxolane monomer. For all PFSF fractions studied, the T_g was much higher (*i.e.*, 60-140°C) than the thermal transition observed in the Nafion sulfonyl precursor (*i.e.*, 0°C).

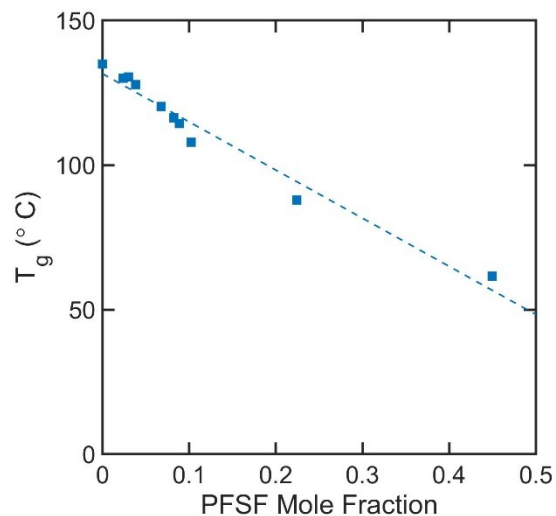


Figure 6: T_g of the sulfonyl-fluoride precursor to PFMMD-co-PFSA for sulfonated monomer mole fractions ranging from 0 to 0.45 as measured by DSC. T_g depressed sharply with increased PFSA fraction but was much higher than the T_g of the Nafion PFSA precursor (0°C) for all compositions. This indicates that incorporation of PFMMD in the ionomer resulted in inhibition of matrix segmental motion, which is reflected in the reduction of ionomer domain spacing, proton conductivity, and water sorption.

Despite the high T_g of PFMMD homopolymers, this class of polymers exhibit higher permeability than PTFE due to their lower density (*i.e.*, 1.959 g cm⁻³ in contrast with 2.2 g cm⁻³ for PTFE), which results in a high fractional free volume (FFV) of 0.23²⁵. In the case of PFMMD-co-PFSA ionomers, we find a density decrease between 5 to 7% with respect to Nafion. This small density change has significant implications for the FFV of the polymers, which increases by up to 21% upon incorporation of an amorphous PFMMD matrix. The substantial increase in FFV resulted in a >240% increase in permeability with respect to Nafion, as demonstrated in Figure 8 for H₂, O₂, Ar, and CO₂. While the overall permeability of PFMMD-co-PFSA was much higher than Nafion, the selectivity towards each gas was similar. The change in backbone chemistry did not appear to significantly alter the nature of polymer/gas interactions. Furthermore, the permeability showed no clear dependence on chain composition, as it remained largely unchanged as a function of PFSA concentration. This supports the assertion that FFV contributions, which did

not show compositional dependence, strongly dominate over chain mobility. These results are consistent with the behavior of PTFE-based ionomers, where gas permeation occurs primarily through the matrix when dehydrated.

Material		Density (g cm^{-3})	FFV
PFMMD-co-PFSA	57%	1.86 ± 0.08	0.260 ± 0.030
PFSA			
PFMMD-co-PFSA	37%	1.86 ± 0.02	0.260 ± 0.010
PFSA			
PFMMD-co-PFSA	26%	1.89 ± 0.01	0.249 ± 0.004
PFSA			
Nafion 40% PFSA		2.005 ± 0.002	0.215 ± 0.001

Table 1: Density (g cm^{-3}) and FFV for PFMMD-co-PFSA compositions and Nafion 1100. 120 nm films were cast on 10 MHz AT-cut Quartz Crystal Microbalance (QCM) crystals with Au electrodes and area densities were measured with dry N_2 flow. Film thicknesses were measured by ellipsometry under the same conditions to calculate volumetric density. All compositions of PFMMD-co-PFSA showed lower density and higher FFV, indicating improved permeability.

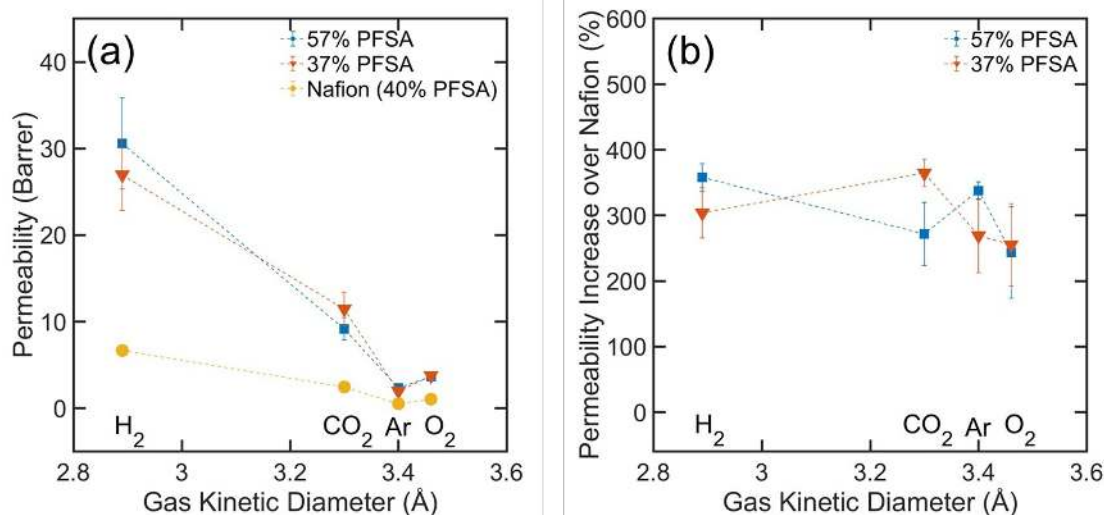


Figure 7: Permeability of dehydrated PFMMD-co-PFSA was several times higher than Nafion towards a range of gases including H_2 , O_2 , Ar, and CO_2 . The high permeability is attributed to the increased FFV upon incorporation of PFMMD into the ionomer matrix. Measurements were performed on PTFE-supported ionomer films of 1 μm thickness in a constant-volume permeation cell.

Performance of PFMMD-co-PFSA ionomers in Membrane Electrode Assemblies

Overall ionomer performance as a catalyst binder is determined by its ability to facilitate the transport of gases (O₂, H₂) and protons in the catalyst layer (CL). PFMMD-co-PFSA ionomers exhibit a tradeoff between higher gas permeability and restricted proton conductivity, with respect to Nafion ionomers. To understand the implications in PEFC performance of this tradeoff, catalyst-coated membranes were constructed employing either (i) PFMMD-co-PFSA (0.57 PFSA fraction) or (ii) Nafion as catalyst binder at the working electrode with loading of 0.1 mg Pt cm⁻² sprayed onto Nafion (NR212) membrane. No delamination or unanticipated contact resistances were observed, and the novel ionomer did not require any additional processing considerations. The counter electrode loading was a gas-diffusion electrode fixed at 0.3 mg Pt cm⁻² with Nafion as catalyst binder. Electrochemical performance of PFMMD-co-PFSA was evaluated by two techniques. First, mass-transport resistance of the respective ionomer films was determined by operating the membrane-electrode assembly as a hydrogen pump (*i.e.*, oxidation of H₂ gas at the working electrode and reduction of H⁺ at the counter electrode). This configuration has a number of advantages that have enabled improved understanding and modeling of catalyst-layer transport resistances³⁹⁻⁴², since the local environment is easier to control (relative to oxygen reduction in a PEFC cathode) given the lack of oxide formation and generation of water and heat. Using very dilute H₂, the mass-transport limit can be achieved at low current density, ensuring minimal ohmic losses. At limiting current density, the H₂-transport resistance in the catalyst layer is given by

$$R_{CL} = 2F c_{H_2} \lim_{j \rightarrow j_{lim}} \frac{L}{3D_{CL}} + \frac{1}{r_f} R_{Local} \frac{1}{r_f} R_{Local} j \quad \text{(Equation 6)}$$

where F is Faraday's constant, C_{H_2} is the concentration of H_2 in the feed, i_{lim} is the limiting current density, L is the catalyst-layer thickness, D_{CL} is the effective reactant gas diffusivity in the catalyst-layer pores, r_f is the roughness factor or the normalized electrochemically active surface area (ECSA), and R_{Local} is the local H_2 -transport resistance contributed by ionomer thin film on/near Pt⁴¹. The first term

$(\frac{L}{3D_{CL}})$ represents transport resistance through CL secondary pores and the second term is the normalized local H_2 -transport resistance. Catalyst loading is proportional directly to L and inversely to r_f , so the first term is negligible at low loading. The results (Figure 9a) show a marked decrease in transport resistance for the catalyst layer employing PFMMD-co-PFSA. This confirms that the introduction of PFMMD to the ionomer matrix successfully improved gas transport during electrochemical operation. It is important to note that this device is operated at 80% humidity, whereas permeability measurements were taken in the dry state. The fact that the improvement in gas transport persists at high humidity is promising for implementation in electrochemical systems and a successful demonstration of deconvoluting ionic and gas-transport pathways.

The reduced transport resistance exhibited in PFMMD-based catalyst layers is expected to improve PEFC performance. Figure 9b shows the normalized polarization performance when running the same assemblies in fuel-cell mode with H_2 at the counter electrode and air at the working electrode. From the curves, the PFMMD-based ionomer with 57% PFSA catalyst layer exhibited superior performance compared to Nafion. This is despite reduced proton conductivity in the

PFMMD-co-PFSA ionomer, underscoring the value of high permeability in ionomers for PEFC catalyst binders. Per cm^2 of Pt, this MEA achieved 22% higher current density at 0.25V than the device employing Nafion. In fact, improved performance throughout the whole polarization curve and not just in the mass-transport dominated part is witnessed, which also hints that the PFMMD-co-PFSA ionomer and its increased FFV helps to inhibit catalyst poisoning by sulfonic-acid moieties more so than the linear backbone of Nafion.

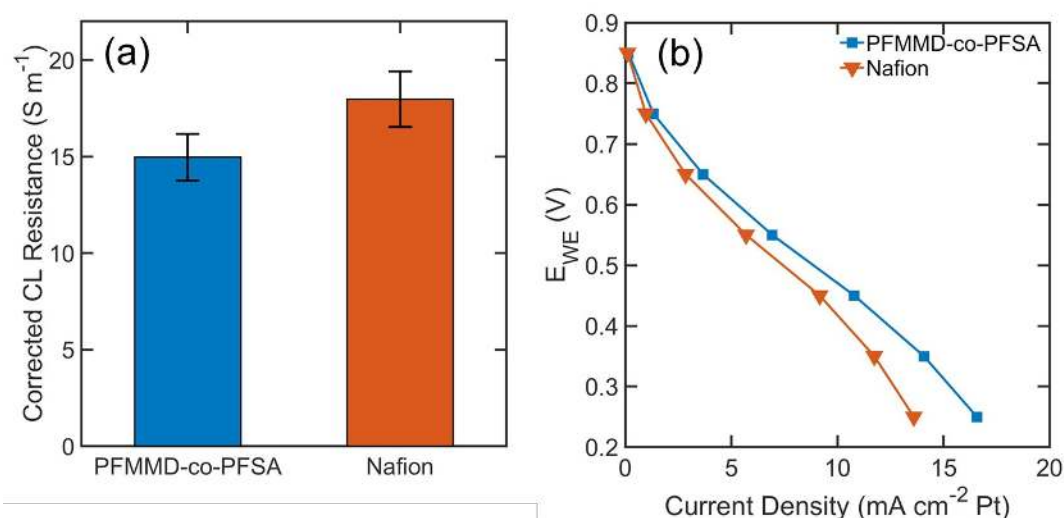


Figure 8: (a) Catalyst layer transport resistance in low-catalyst loading MEA's employing PFMMD-co-PFSA (57% PFSA) and Nafion determined by limiting current density measurements in oxidation of H_2 . PFMMD-co-PFSA displayed reduced transport resistance attributed to increase of free volume in the ionomer matrix. (b) Polarization curves of the same MEA's operated as fuel cells in H_2/air . Adjusting current density by the ECSA shows higher current per cm^2 Pt in PFMMD-based ionomer than Nafion.

Conclusions

This study demonstrated a new family of perfluorinated ionomers, PFMMD-co-PFSA, molecularly designed to enhance transport properties of catalyst layers. The ionomer chemical structure leads to an amorphous glassy matrix designed to impart high gas permeability and keep the sulfonic-acid moieties from the surface, while maintaining similar proton conduction pathways to state-of-the-art PFSA

ionomers. The free-radical polymerization of this ionomer exhibited large differences in reactivity ratios between the two monomers, $r_{\text{PFMMD}} \gg 1 > r_{\text{PFSVE}}$, which required the development of a numerical model to map synthesis parameters leading to statistical random copolymers with low compositional drifts. The synthesized ionomers displayed reduced water sorption and conductivity compared to traditional PFSA, which may be attributed to the low mobility of the glassy PFMMD matrix. This was consistent with results from SAXS/WAXS measurements that revealed smaller ionomer domains with a more amorphous matrix in PFMMD-based ionomers than Nafion. However, the increased FFV of the ionomer matrix led to higher gas permeability. The tradeoff between lower proton conductivity and enhanced gas transport was assessed by determining the transport resistance and electrochemical performance in electrodes with PFMMD-co-PFSA functional binders. Thanks to their high conductivity and gas permeability, catalyst layers fabricated with PFMMD-co-PFSA ionomers with high sulfonic-acid content demonstrated enhanced fuel-cell performance (i.e., up to 22% increase in current density at a given potential) per active surface area with respect to those fabricated with Nafion. These promising results demonstrate the importance of rationally designed ionomers, such as the ones presented in this study, to achieve higher performing electrochemical devices, especially at low Pt loading. Future studies should explore PFMMD-co-PFSA catalyst ink formulations and deposition methods to obtain electrodes with high active surface areas and ultimately exploit the advantages of this new generation of ionomers.

Experimental

Synthesis of PFMMMD-co-PFSA Ionomers

PFSVE was purchased from Synquest Laboratories, Inc. Hexafluorobenzene (HFB) was purchased from Sigma Aldrich. Perfluorobenzoyl peroxide (PFBPO), used as initiator, was prepared by reaction of pentafluoro benzoyl chloride with hydrogen peroxide. The crude PFBPO product was crystallized from methanol/chloroform mixture (2:1 by volume) and had a melting point of 76-78°C. The preparation of PFMMMD was previously reported^{43,44}. All other chemicals were purchased from Sigma-Aldrich. PFMMMD, PFSVE, and PFBPO were dissolved in HFB and added to a thick-walled glass ampoule (Chemglass Life Sciences). The reaction mixture was degassed by three freeze-pump-thaw cycles with liquid nitrogen. The ampoule was sealed under vacuum and heated to 60°C to initiate copolymerization. Reaction times were controlled to keep conversion below the threshold for 25% compositional drift (see Results and Discussion for more information). The resulting polymer was precipitated by dropwise addition to a large excess of dichloromethane. The solid polymer was recovered by vacuum filtration and rinsed thoroughly with dichloromethane to remove unreacted monomers. The product was then dried under vacuum at 70°C for 24 hours and weighed to determine yield, which was used to calculate the approximate conversion. The as-synthesized polymer was in the sulfonyl fluoride ($-\text{SO}_2\text{F}$) form. Polymer composition was determined by elemental analysis conducted by Atlantic Microlab, Inc. with $\pm 0.3\%$ accuracy and precision. This was converted to the sulfonic acid ($-\text{SO}_3^-\text{H}^+$) form by base hydrolysis followed by protonation. Base hydrolysis was performed by preparing a slurry of polymer in strong base (25% (w/w) in H_2O) at 85°C with stirring for 12 hours, which yielded the Na^+ salt form of the ionomer⁴⁵. This product was recovered by vacuum filtration, rinsed with water, and dried under at 70°C vacuum

for 12 hours. The salt form was protonated by adding to sulfuric acid (25% w/w) at 85°C with stirring for 12 hours, then recovered by vacuum filtration, rinsed with DI water, and dried under vacuum at 70 °C for 12 hours.

Nanostructure and Ionic Conductivity

PFMMD-co-PFSA was dissolved at 5% (w/w) in 70% IPA in DI water and spin-cast on silicon substrates yielding films with thicknesses between 120 and 140 nm. Prior to spin-casting, substrates were cleaned by solvent rinsing and O₂/N₂ plasma treatment. Films were annealed for 12 hours at 130°C after spin-casting. Thickness and swelling measurements were taken with a J.A. Woollam Variable Angle Spectroscopic Ellipsometer with a custom-built LabVIEW module for controlling and measuring relative humidity. For conductivity measurements, silicon substrates were patterned with platinum interdigitated microelectrodes (IDEs) fabricated at the City University of New York Advanced Science Research Center. IDEs had platinum teeth of 300 μm length, 5 μm width, 200 nm height (with a 20 nm Ti adhesion layer), and 100 μm spacing. Ohmic contacts between the IDE microelectrodes and potentiostat (Biologic VSP-300) were embedded in sealed glass vials to enable humidity-controlled conductivity measurements. During conductivity measurements, humidity was controlled by adding a reservoir of saturated aqueous salt to the vial⁴⁶. Films were maintained in controlled humidity environment for 24 hours prior to measurement. Film resistance was determined by electrochemical impedance spectroscopy (EIS) and used to calculate ionomer conductivity as

$$\kappa_f = \frac{1}{R_f} \frac{d}{l(N-1)t} \quad \text{(Equation 7)}$$

where κ_f is the film conductivity, R_f is the resistance, t is the film thickness, d is the spacing between IDE teeth, and l is the overlap length of the teeth, and N is the

number of teeth^{47,48}. Impedance spectra were collected from 100 Hz to 7 MHz with an amplitude of 0.10 mV. Ionomer film resistance was extracted from the impedance spectrum by fitting a semicircle to the high-frequency circular feature, following previous analysis of PFSA films on similar IDEs^{33,48-50}.

Ionomer samples were drop-cast from 5 wt% in IPA/H₂O into Kapton-sealed stainless-steel washers with DI water to hydrate the ionomers. SAXS measurements were performed at beamline 7.3.3 of the Advanced Light Source at Lawrence Berkeley National Lab. The X-ray energy was 10 keV with a monochromator resolution E/dE of 100. Scattering patterns were acquired with a 2D Dectris Pilatus 1M CCD area detector (172 μm x 172 μm pixel size). WAXS experiments were performed at the NYU Department of Chemistry Shared Instrumentation Facility. The powder sample was loaded into an 0.8 mm Kapton capillary and then mounted on a magnetic base of the sample stage of a Bruker D8 DISCOVER GADDS microdiffractometer. The instrument is equipped with a VÅNTEC-2000 area detector. The X-ray generated from a sealed Cu tube is monochromated by a graphite crystal and collimated by a 0.5mm MONOCAP ($\lambda_{\text{Cu-K}\alpha} = 1.54178 \text{ \AA}$). The sample-detector distance is set at 150 mm. Scans were collected in a ϕ rotation method and with an exposure time of 600 seconds per scan. The two-dimensional diffraction data were integrated by the XRD2EVAL program in the Bruker PILOT software. The raw file of the powder pattern generated was analyzed by the DIFFRACplus EVA software.

Gas Transport Properties

Differential scanning calorimetry (DSC Q2000, TA Instruments, New Castle, DE) was used to determine the thermal transitions of the polymers at a heating rate of 10 $^{\circ}\text{C min}^{-1}$ under 50 mL min^{-1} N₂ flow. The T_g was determined using Universal

Analysis 2000 software. Density measurements were performed by spin-casting ionomer films on 10 MHz AT-cut quartz-crystal microbalance crystals with evaporated gold electrodes (OpenQCM, nominal sensitivity $4.42 \times 10^{-9} \text{ g Hz}^{-1} \text{ cm}^{-2}$). Film areal density was measured with an OpenQCM Fluidic Cell QCM with dry N_2 flow at room temperature. Film thickness was measured via spectroscopic ellipsometry with dry N_2 flow to calculate ionomer density. FFV was then be calculated as:

$$FFV = 1.3 \rho V_{VDW} \quad (\text{Equation 8})$$

where ρ is the polymer density and V_{VDW} is the van der Waals volume as estimated by the Bondi group contribution method^{51,52}. Ionomer permeability was measured with a constant-volume gas permeation cell. Ionomer films were prepared by spin-casting from solutions of 20 wt% ionomer in IPA/ H_2O on a nanoporous PTFE filter membrane (Whatman #110601, 15 nm pore size). Films were further supported in circular aluminum tape with the area for gas flux removed by die punch and loaded into the permeation cell. Films were degassed under vacuum overnight. Prior to testing, a 15-minute leak test was performed. The test gas was then introduced at 1, 2, 3, and 4 atm for 15 minutes each, with a 2-minute evacuation between pressure steps. Permeability at each pressure step was calculated as:

$$P_A = \frac{V_d I}{p_{up} A R T} \left[\left(\frac{d p_{down}}{dt} \right)_{SS} - \left(\frac{d p_{down}}{dt} \right)_{leak} \right] \quad (\text{Equation 9})$$

where V_d is the downstream volume, I is the polymer film thickness, p_{up} is the upstream test gas pressure, p_{down} is the measured downstream pressure (subscript SS denotes steady-state pressure test of test gas, and leak denotes the pressure rise during the leak test), A is the area of exposed polymer film, R is the ideal gas constant and T is the temperature. All measurements were performed at 35°C controlled by submerging the permeation cell in a water bath.

Electrochemical Performance of PFMMD-co-PFSA

MEAs were fabricated with the following counter electrode (CE) and working electrode (WE) parameters: Pt loading was fixed at 0.1 mg cm^{-2} (WE) and 0.3 mg cm^{-2} (CE), with 30 wt% Pt/Vulcan (WE) and 50 wt% Pt/Vulcan (CE), and 0.8 (WE) and 0.9 (CE) ionomer-carbon ratio. Nafion was used as binder at both CEs, while one MEA was fabricated with PFMMD-co-PFSA (0.57 PFSA mass fraction) as the WE binder and the other with Nafion. Electrodes were sprayed on Nafion NR212 (WE) and Sigracet 25BC GDL (CE). Active surface area was measured via CO stripping at 40°C , 80% RH, and ambient pressure in cell hardware with an active area of 2 cm^2 . The catalyst-layer transport resistance was determined by limiting current towards H_2 oxidation at 40°C , 80% RH in the same cell hardware, with 1000 ppm H_2 flow at the WE and 2% H_2 balance Ar at the CE. Limiting current was measured at a constant potential of 0.3 V. Polarization curves were again obtained at 40°C , 80% RH, and ambient pressure, with air flow at the WE and H_2 at the CE. Potential was varied from 0.85V to 0.25V at 5-minute intervals of 0.1V. Current was averaged over the last two minutes. Complete details of cell assembly and testing conditions can be found in reference 41.

Acknowledgements

This material is based upon work supported by the U.S. Department of Energy, Office of Science, Office of Workforce Development for Teachers and Scientists, Office of Science Graduate Student Research (SCGSR) program. The SCGSR program is administered by the Oak Ridge Institute for Science and Education

(ORISE) for the DOE. ORISE is managed by ORAU under contract number DE-SC0014664.

This work was performed in part at the Advanced Science Research Center NanoFabrication Facility of the Graduate Center at the City University of New York.

This research used resources of the Advanced Light Source, which is a DOE Office of Science User Facility under contract no. DE-AC02-05CH11231.

This research used beamline 11BM (CMS) of the National Synchrotron Light Source II and the Center for Functional Nanomaterials (CFN), U.S. Department of Energy (DOE) Office of Science User Facilities operated for the DOE Office of Science by Brookhaven National Laboratory under Contract No. DE-SC0012704. We thank Dr. Esther Tsai and Dr. Ruipeng Li for their assistance performing experiments at beamline CMS. We thank Dr. Chunhua T. Hu at the X-ray Diffraction Facility of NYU Department of Chemistry for his help. C.T.H. acknowledges the support of the National Science Foundation (NSF) Chemistry Research Instrumentation and Facilities Program (CHE-0840277) and Materials Research Science and Engineering Center (MRSEC) Program (DMR-1420073).

We thank Mr. Peter Dudenas, Dr. Meron Tesfaye, and Dr. Douglas Kushner for facilitating SAXS experiments, permeability measurements, and many insightful discussions.

References

- (1) U.S. Department of Energy office of Energy Efficiency and Renewable Energy. Hydrogen Storage <https://www.energy.gov/eere/fuelcells/hydrogen-storage> (accessed May 6, 2019).
- (2) Weber, A. Z.; Newman, J. Modeling Transport in Polymer-Electrolyte Fuel Cells. *Chem. Rev.* **2004**, *104* (10), 4679–4726. <https://doi.org/10.1021/cr020729l>.

- (3) Mauritz, K. A.; Moore, R. B. State of Understanding of Nafion. *Chem. Rev.* **2004**, *104* (10), 4535–4585. <https://doi.org/10.1021/cr0207123>.
- (4) Grot, W. DISCOVERY AND DEVELOPMENT OF NAFION PERFLUORINATED MEMBRANES. *Chem. Ind.* **1985**, 647–649.
- (5) Kusoglu, A.; Weber, A. Z. New Insights into Perfluorinated Sulfonic-Acid Ionomers. *Chem. Rev.* **2017**, *117* (3), 987–1104. <https://doi.org/10.1021/acs.chemrev.6b00159>.
- (6) Rollet, A. L.; Diat, O.; Gebel, G. A New Insight into Nafion Structure. *J. Phys. Chem. B* **2002**, *106* (12), 3033–3036. <https://doi.org/10.1021/jp020245t>.
- (7) Kreuer, K. D.; Portale, G. A Critical Revision of the Nano-Morphology of Proton Conducting Ionomers and Polyelectrolytes for Fuel Cell Applications. *Adv. Funct. Mater.* **2013**, *23* (43), 5390–5397. <https://doi.org/10.1002/adfm.201300376>.
- (8) Kusoglu, A.; Dursch, T. J.; Weber, A. Z. Nanostructure/Swelling Relationships of Bulk and Thin-Film PFSA Ionomers. *Adv. Funct. Mater.* **2016**, *26* (27), 4961–4975. <https://doi.org/10.1002/adfm.201600861>.
- (9) Allen, F. I.; Comolli, L. R.; Kusoglu, A.; Modestino, M. A.; Minor, A. M.; Weber, A. Z. Morphology of Hydrated As-Cast Nafion Revealed through Cryo Electron Tomography. *ACS Macro Lett.* **2015**, *4* (1), 1–5. <https://doi.org/10.1021/mz500606h>.
- (10) Ollivier, J.; Guillermo, A.; Berrod, Q.; Lyonnard, S.; Manseri, A.; Gébel, G.; Frick, B.; Améduri, B. Nanostructure and Transport Properties of Proton Conducting Self-Assembled Perfluorinated Surfactants: A Bottom-Up Approach toward PFSA Fuel Cell Membranes. *Macromolecules* **2015**, *48* (17), 6166–6176. <https://doi.org/10.1021/acs.macromol.5b00770>.
- (11) Mukaddam, M.; Wang, Y.; Pinnau, I. Structural, Thermal, and Gas-Transport Properties of Fe³⁺ Ion-Exchanged Nafion Membranes. *ACS Omega* **2018**, *3* (7), 7474–7482. <https://doi.org/10.1021/acsomega.8b00914>.
- (12) Michaels A. S.; Bixler H. J. Solubility of Gases in Polyethylene. *J. Polym. Sci.* **1961**, *L*, 393–412. <https://doi.org/10.1002/0470867833.ch4>.
- (13) Mukaddam, M.; Litwiller, E.; Pinnau, I. Gas Sorption, Diffusion, and Permeation in Nafion. *Macromolecules* **2016**, *49* (1), 280–286. <https://doi.org/10.1021/acs.macromol.5b02578>.
- (14) Evans, C. M.; Singh, M. R.; Lynd, N. A.; Segalman, R. A. Improving the Gas Barrier Properties of Nafion via Thermal Annealing: Evidence for Diffusion through Hydrophilic Channels and Matrix. *Macromolecules* **2015**, *48* (10), 3303–3309. <https://doi.org/10.1021/acs.macromol.5b00579>.
- (15) Lee, K.; Ishihara, A.; Mitsushima, S.; Kamiya, N.; Ota, K. Effect of Recast Temperature on Diffusion and Dissolution of Oxygen and Morphological Properties in Recast Nafion. *J. Electrochem. Soc.* **2004**, *151* (4), A639. <https://doi.org/10.1149/1.1652052>.
- (16) Kusoglu, A.; Savagatrup, S.; Clark, K. T.; Weber, A. Z. Role of Mechanical

- Factors in Controlling the Structure-Function Relationship of PFSA Ionomers. *Macromolecules* **2012**, 45 (18), 7467–7476.
<https://doi.org/10.1021/ma301419s>.
- (17) Page, K. A.; Cable, K. M.; Moore, R. B. Molecular Origins of the Thermal Transitions and Dynamic Mechanical Relaxations in Perfluorosulfonate Ionomers. *Macromolecules* **2005**, 38 (15), 6472–6484. <https://doi.org/10.1021/ma0503559>.
 - (18) Litster, S.; McLean, G. PEM Fuel Cell Electrodes. *J. Power Sources* **2004**, 130 (1-2), 61–76. <https://doi.org/10.1016/j.jpowsour.2003.12.055>.
 - (19) Wang, L.; Husar, A.; Zhou, T.; Liu, H. A Parametric Study of PEM Fuel Cell Performances. *Int. J. Hydrogen Energy* **2003**, 28 (11), 1263–1272.
[https://doi.org/10.1016/S0360-3199\(02\)00284-7](https://doi.org/10.1016/S0360-3199(02)00284-7).
 - (20) Weber, A. Z.; Kusoglu, A. Unexplained Transport Resistances for Low-Loaded Fuel-Cell Catalyst Layers. *J. Mater. Chem. A* **2014**, 2 (41), 17207–17211.
<https://doi.org/10.1039/c4ta02952f>.
 - (21) Sauguet, L.; Ameduri, B.; Boutevin, B. Fluorinated Copolymers and Terpolymers Based on Vinylidene Fluoride and Bearing Sulfonic Acid Side-Group. *J. Polym. Sci. Part A Polym. Chem.* **2007**, 45, 1814–1834.
<https://doi.org/10.1002/pola>.
 - (22) Rolfi, A.; Oldani, C.; Merlo, L.; Facchi, D.; Ruffo, R. New Perfluorinated Ionomer with Improved Oxygen Permeability for Application in Cathode Polymeric Electrolyte Membrane Fuel Cell. *J. Power Sources* **2018**, 396 (May), 95–101.
<https://doi.org/10.1016/j.jpowsour.2018.05.093>.
 - (23) Koike, K.; Mikeš, F.; Zhang, H.; Koike, Y.; Okamoto, Y. Synthesis and Characterization of Copolymers of Perfluoro(2-Methylene-4,5-Dimethyl-1,3-Dioxolane) and Perfluoro(2-Methylene-1,3-Dioxolane). *J. Fluor. Chem.* **2013**, 156, 198–202. <https://doi.org/10.1016/j.jfluchem.2013.10.001>.
 - (24) Pasternak, R. A.; Christensen, V.; Heller, J. Diffusion and Permeation of Oxygen, Nitrogen, Carbon Dioxide, and Nitrogen Dioxide through Polytetrafluoroethylene. *Macromolecules* **1970**, 3 (3), 366–371.
<https://doi.org/10.1021/ma60015a020>.
 - (25) Yavari, M.; Fang, M.; Nguyen, H.; Merkel, T. C.; Lin, H.; Okamoto, Y. Dioxolane-Based Perfluoropolymers with Superior Membrane Gas Separation Properties. *Macromolecules* **2018**, 51 (7), 2489–2497.
<https://doi.org/10.1021/acs.macromol.8b00273>.
 - (26) Fang, M.; Chiang, H. C.; Okamoto, Y. Mechanical and Optical Properties of the Copolymers of Perfluoro(2-Methylene-4-Methyl-1,3-Dioxolane) and Chlorotrifluoroethylene. *J. Fluor. Chem.* **2018**, 214 (August), 63–67.
<https://doi.org/10.1016/j.jfluchem.2018.08.001>.
 - (27) Fang, M.; He, Z.; Merkel, T. C.; Okamoto, Y. High-Performance Perfluorodioxolane Copolymer Membranes for Gas Separation with Tailored Selectivity Enhancement. *J. Mater. Chem. A* **2018**, 6 (2), 652–658.
<https://doi.org/10.1039/c7ta09047a>.

- (28) Rudin, A.; Choi, P. *The Elements of Polymer Science and Engineering*, 3rd ed.; Academic Press: Waltham, MA, 2013.
- (29) Mayo, F. R.; Lewis, F. M. A Basis for Comparing the Behavior of Monomers in Copolymerization; The Copolymerization of Styrene and Methyl Methacrylate. *J. Am. Chem. Soc.* **1944**, 66 (9), 1594–1601.
<https://doi.org/10.1021/ja01237a052>.
- (30) Skeist, I. Copolymerization: The Composition Distribution Curve. *J. Am. Chem. Soc.* **1946**, 68 (9), 1781–1784. <https://doi.org/10.1021/ja01213a031>.
- (31) Meyer, V. E.; Lowry, G. G. Integral and Differential Binary Copolymerization Equations. *J. Polym. Sci. Part A Gen. Pap.* **2003**, 3 (8), 2843–2851.
<https://doi.org/10.1002/pol.1965.100030811>.
- (32) Gierke, T. D.; Munn, G. E.; Wilson, F. C. The Morphology in Nafion Perfluorinated Membrane Products, as Determined by Wide- and Small-Angle x-Ray Studies. *J. Polym. Sci. Polym. Phys. Ed.* **1981**, 19 (11), 1687–1704.
<https://doi.org/10.1002/pol.1981.180191103>.
- (33) Modestino, M. A.; Paul, D. K.; Dishari, S.; Petrina, S. A.; Allen, F. I.; Hickner, M. A.; Karan, K.; Segalman, R. A.; Weber, A. Z. Self-Assembly and Transport Limitations in Confined Nafion Films. *Macromolecules* **2013**, 46, 867–873.
<https://doi.org/10.1021/ma301999a>.
- (34) Kusoglu, A.; Modestino, M. A.; Hexemer, A.; Segalman, R. A.; Weber, A. Z. Subsecond Morphological Changes in Nafion during Water Uptake Detected by Small-Angle X-Ray Scattering. *ACS Macro Lett.* **2012**, 1 (1), 33–36.
<https://doi.org/10.1021/mz200015c>.
- (35) Fujimura, M.; Hashimoto, T.; Hawaii, H. Small-Angle X-Ray Scattering Study of Perfluorinated Ionomer Membranes. 1. Origin of Two Scattering Maxima. *Macromolecules* **1981**, 14 (5), 1309–1315.
<https://doi.org/10.1021/ma50006a032>.
- (36) Araki, Y. Thermal Expansion Coefficient of Polytetrafluoroethylene in the Vicinity of Its Glass Transition at about 400°K. *J. Appl. Polym. Sci.* **1965**, 9 (2), 421–427. <https://doi.org/10.1002/app.1965.070090203>.
- (37) de Almeida, S. H.; Kawano, Y. Thermal Behavior of Nafion Membrane. *J. Therm. Anal. Calorim.* **1999**, 58, 569–577.
<https://doi.org/10.1023/A:1010196226309>.
- (38) Tesfaye, M.; Kushner, D. I.; McCloskey, B. D.; Weber, A. Z.; Kusoglu, A. Thermal Transitions in Perfluorosulfonated Ionomer Thin-Films. *ACS Macro Lett.* **2018**, 7, 1237–1242. <https://doi.org/10.1021/acsmacrolett.8b00628>.
- (39) Freiberg, A. T. S.; Tucker, M. C.; Weber, A. Z. Polarization Loss Correction Derived from Hydrogen Local-Resistance Measurement in Low Pt-Loaded Polymer-Electrolyte Fuel Cells. *Electrochem. commun.* **2017**, 79 (April), 14–17.
<https://doi.org/10.1016/j.elecom.2017.04.008>.
- (40) Spingler, F. B.; Phillips, A.; Schuler, T.; Tucker, M. C.; Weber, A. Z. Investigating Fuel-Cell Transport Limitations Using Hydrogen Limiting Current. *Int. J. Hydrogen Energy* **2017**, 42 (19), 13960–13969.

<https://doi.org/10.1016/j.ijhydene.2017.01.036>.

- (41) Schuler, T.; Chowdhury, A.; Freiberg, A. T.; Sneed, B.; Spingler, F. B.; Tucker, M. C.; More, K. L.; Radke, C. J.; Weber, A. Z. Fuel-Cell Catalyst-Layer Resistance via Hydrogen Limiting-Current Measurements. *J. Electrochem. Soc.* **2019**, *166* (7), F3020–F3031. <https://doi.org/10.1149/2.0031907jes>.
- (42) Chowdhury, A.; Radke, C. J.; Weber, A. Z. Transport Resistances in Fuel-Cell Catalyst Layers. *ECS Trans.* **2017**, *80* (8), 321–333. <https://doi.org/10.1149/08008.0321ecst>.
- (43) Mikeš, F.; Yang, Y.; Teraoka, I.; Ishigure, T.; Koike, Y.; Okamoto, Y. Synthesis and Characterization of an Amorphous Perfluoropolymer: Poly(Perfluoro-2-Methylene-4-Methyl-1,3-Dioxolane). *Macromolecules* **2005**, *38* (10), 4237–4245. <https://doi.org/10.1021/ma050085u>.
- (44) Selman, S.; Squire, E. N. US Patent Number 3,308,107, 1919.
- (45) Cisar, A. J. US Patent No. 6,495,209 B1, 2002. <https://doi.org/10.1145/634067.634234>.
- (46) Greenspan, L. Humidity Fixed Points of Binary Saturated Aqueous Solutions. *J. Res. Natl. Bur. Stand. Sect. A Phys. Chem.* **1977**, *81A* (1), 89. <https://doi.org/10.6028/jres.081A.011>.
- (47) Paul, D. K.; McCreery, R.; Karan, K. Proton Transport Property in Supported Nafion Nanothin Films by Electrochemical Impedance Spectroscopy. *J. Electrochem. Soc.* **2014**, *161* (14), F1395–F1402. <https://doi.org/10.1149/2.0571414jes>.
- (48) Paul, D. K.; Karan, K.; Docoslis, A.; Giorgi, J. B.; Pearce, J. Characteristics of Self-Assembled Ultrathin Nafion Films. *Macromolecules* **2013**, *46* (9), 3461–3475. <https://doi.org/10.1021/ma4002319>.
- (49) Paul, D. K.; Fraser, A.; Karan, K. Towards the Understanding of Proton Conduction Mechanism in PEMFC Catalyst Layer: Conductivity of Adsorbed Nafion Films. *Electrochem. commun.* **2011**, *13* (8), 774–777. <https://doi.org/10.1016/j.elecom.2011.04.022>.
- (50) Paul, D.; Fraser, A.; Pearce, J.; Karan, K. Understanding the Ionomer Structure and the Proton Conduction Mechanism in PEFC Catalyst Layer: Adsorbed Nafion on Model Substrate. *ECS Trans.* **2011**, *41* (1), 1393–1406. <https://doi.org/10.1149/1.3635670>.
- (51) Van Krevelen, D. W.; te Nijenhuis, K. *Properties of Polymers*, 4th ed.; Elsevier: Amsterdam, 2009. <https://doi.org/10.1016/B978-0-444-82877-4.50011-1>.
- (52) Bondi, A. Van Der Waals Volumes and Radii. *J. Phys. Chem.* **1964**, *68* (3), 441–451. <https://doi.org/10.1021/j100785a001>.